GEOPHYSICS, VOL. 79, NO. 5 (SEPTEMBER-OCTOBER 2014); P. D275–D287, 12 FIGS., 3 TABLES.
10.1190/GEO2013-0167.1

Diagnostics of seismic time-lapse effects of sandstones based on laboratory data

Bernardo Moyano[1], Tor Arne Johansen[1], Remy Sverre Agersborg[2], and Kyle T. Spikes[3]

ABSTRACT

We evaluated a viscoelastic modeling of P- and S-wave velocity dispersion, attenuation, pressure, and fluid effects for a set of siliciclastic rock samples. Our analysis used a published laboratory data set of 63 sandstones with a wide range of compositional heterogeneities. We observed a notable correlation between the (velocity and attenuation) pressure sensitivity and the abundance/lack of quartz in the samples. We included compliant pores (low-aspect ratio) proportionally to the content of secondary minerals to account for the differential sensitivity to pressure. The observed velocity and attenuation were well reproduced by the applied viscoelastic modeling. We found that pores of significantly different scale required pore fluid relaxation time constants of proportionally different magnitudes to reproduce the velocity and attenuation measurements. The relaxation time constant of crack-sized pores can be one order of magnitude smaller than the constant of mesopores. Moreover, the velocity dispersion and attenuation signatures revealed that a pore textural model dependent on lithological composition is critical in the prediction of time-lapse fluid and pressure responses.

INTRODUCTION

Understanding how seismic parameters vary with changes in mixing conditions of the pore fluids and pore pressure is crucial for using repeated seismic data (time-lapse seismic) to monitor in situ spatial and temporal variations of the pore fluid composition during either production of hydrocarbons or sequestration of carbon dioxide. The sensitivity of seismic parameters to changes in these reservoir conditions depends, aside from the lithological composition itself, upon the porosity and the pore space topology. Seismic velocities measured in the laboratory are usually obtained at frequencies up to four magnitudes above those used in static and dynamic seismic reservoir characterization. To apply ultrasonic-derived fluid and pressure sensitivity of reservoir rocks for interpretation of the seismic data, we thus need to correct for velocity dispersion effects (Gueguen et al., 2011; Gueguen and Sarout, 2011). Velocity dispersion can, however, occur due to reservoir heterogeneities larger than the core scale but considerably less than the seismic wavelength and due to pore fluid flow generally causing a stiffening of the rock with increasing frequency (Cleary, 1977). This latter dispersion effect can be estimated if the composition of the rock specimen is known together with ultrasonic velocity and attenuation data in combination with an appropriate viscoelastic rock-physics model (Jones, 1986). Velocity dispersion due to pore fluid flow strongly depends on the texture of the pore space, which again also governs how seismic velocities change with altered pore pressure (effective pressure).

Sandstones are composed of quartz, feldspar, clay minerals, and many other naturally occurring minerals. The abundance of a particular mineral in sandstone depends on the availability in the provenance of sediments and also on the stability of that mineral to the weathering and erosive processes (Tucker, 1991). These complexities in composition affect the elastic behavior of the rocks by increasing the complexity of the grain-to-grain contacts and the topology of the pore space. Most effective medium models used for prediction of P- and S-wave velocities of siliciclastic rocks do not include dispersion effects caused by attenuation related to pore fluid flow. However, the viscoelastic model of Jakobsen et al. (2003a, 2003b) and Jakobsen and Johansen (2005) provides a unified approach that includes velocity perturbations caused by interpore fluid flow, pressure, and frequency.

In this paper, we analyze the potential of using this approach to derive parameters of the pore space topology and fluid flow, which provide modeled velocity and attenuation data consistent with measured data of clean and heterogeneous saturated sandstones

Manuscript received by the Editor 26 April 2013; revised manuscript received 20 April 2014; published online 21 July 2014.
[1]University of Bergen, Department of Earth Science, Bergen, Norway. E-mail: rnardo.moyano@wintershall.com; torarne.johansen@geo.uib.no.
[2]Octio AS, Bergen, Norway. E-mail: remy@agersborg.com.
[3]University of Texas at Austin, Geological Sciences, Austin, Texas, USA. E-mail: kyle.spikes@jsg.utexas.edu.

for various pressures. Our implementation of the model serves as a generalization of the dual-porosity model of Xu and White (1995) by considering viscoelastic properties of clay-sand mixtures in which secondary minerals and cracks are added. The modeling procedure is reviewed on the basis of a comprehensive laboratory data set of sandstones (Han et al., 2011a; 2011b) with measurements of P- and S-wave velocities and attenuation.

DATA SET AND OBSERVATIONS

For the analysis, we used a set of recently published laboratory measurements of 63 brine-saturated sandstone samples taken from boreholes and quarries in the UK and China covering a wide range of petrophysical properties (Han et al., 2011a; 2011b). The data set consists of P- and S-wave velocity and attenuation measurements at ultrasonic frequencies and effective pressures varying between 8 and 60 MPa. Additionally, the samples are fully characterized by x-ray diffraction mineralogical analysis, porosity, and permeability measurements by the helium porosimeter and nitrogen gas permeameter, respectively.

With invariant pore fluid, the V_P/V_S ratio depends on lithological composition (Tatham, 1982) and for sands on the degree of consolidation (Dvorkin and Nur, 1996) in which poorly consolidated sediments usually show values larger than ~1.88 (Blangy, 1992). The V_P/V_S and $(Qp/Qs)^{-1}$ ratios versus pressure for the 63 samples are shown in Figure 1 colored by the volume fraction of quartz. It is apparent that the samples with the largest content of quartz show the lowest V_P/V_S ratios. This relates to the dominant effect of the low V_P/V_S ratio of the load-bearing and cemented quartz grains, but it can also indicate that different mineral constituents imply an intrinsically different pore aspect ratio spectrum. Most importantly, this suggests that the degree of consolidation (or cementation) is related to mineralogy. Crossplots between the V_P/V_S ratio and all the petrophysical properties are shown in Figure 2. The relation between the V_P/V_S ratio and mineralogy is again evident. Correlation coefficients (r) between V_P/V_S ratio and the petrophysical parameters (Table 1) show the highest correlation for quartz content ($r = -0.74$). A similar trend for the attenuation $(Qp/Qs)^{-1}$ ratio versus mineralogy is, however, not obvious, and the highest correlation coefficient is $r = -0.29$ when calcite is present together with quartz, clay, and feldspars.

P- and S-wave velocity and attenuation normalized by values obtained at highest effective pressure (60 MPa) are shown in Figure 3. The data are colored by volume fraction of quartz. It is noticeable that the highest pressure sensitivity is shown by the samples with the lowest content of quartz, with a few exceptions. In other words, clean sandstones seem to be stiffer and less pressure-sensitive than the heterogeneous (shaly) sandstones. This trend appears to be more consistent for the P-wave velocity than for the S-wave velocity. In the analysis, we have used data from all the 63 samples as listed in the original publication (Han et al., 2011a). However, because some data overlap, they are not directly visible to the naked eye in the plots shown. The relative significant link between the pressure dependencies of velocity and, to some extent, attenuation to lithological composition as displayed in the data, suggests that the pore texture associated with grain contacts and pore shapes, may be characterized on the basis of mineralogical composition. In the same context as Xu and White (1995), we describe the pore texture with the use of ellipsoidal inclusions in which two dominant textures are

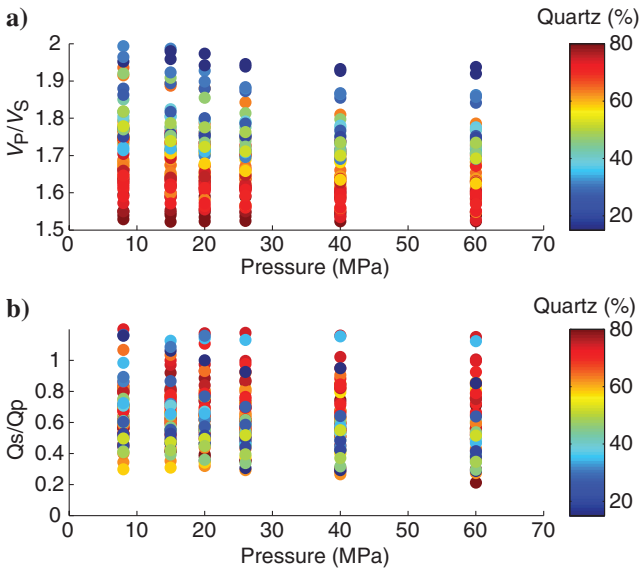

Figure 1. The (a) V_P/V_S ratio versus pressure and (b) $(Qp/Qs)^{-1}$ ratio versus pressure colored by quartz content, of the 63 sandstone samples analyzed by Han et al. (2011a). The samples with the greater quartz content (clean sandstones) show lower V_P/V_S values. Conversely, the samples with a lower quartz content (heterogeneous sandstones) show larger V_P/V_S values. The attenuation $(Qp/Qs)^{-1}$ ratio does not show a similar trend.

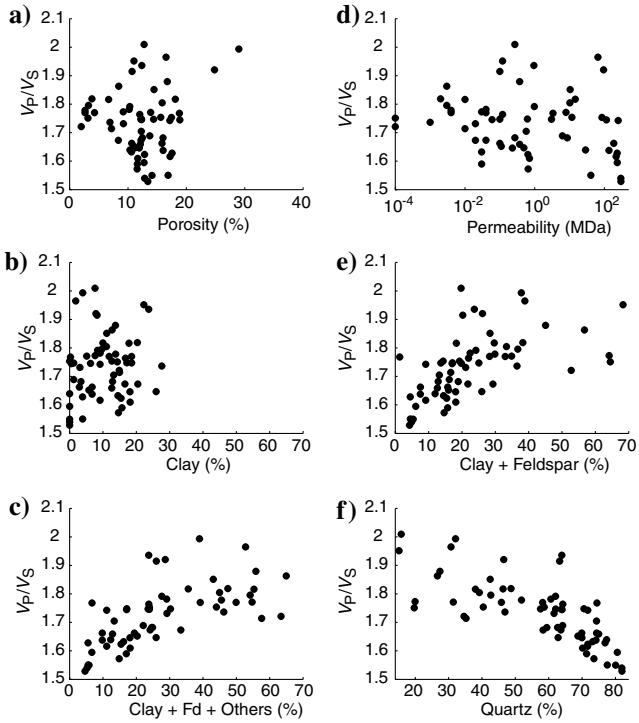

Figure 2. Crossplots between V_P/V_S and petrophysical properties and mineral content for the 63 sandstone samples analyzed by Han et al. (2011a). The V_P/V_S (a) versus porosity, (b) versus clay content, (c) versus clay + feldspar + other minerals, (d) versus permeability, (e) versus clay + feldspar content, and (f) versus quartz content. Note the strong correlation (inverse) between V_P/V_S and quartz content seen in (f).

considered, one representing the aggregate of quartz and one representing the remaining minerals.

The main objective of our study is to show how viscoelastic rock-physics modeling can be used to link pressure signatures of ultrasonic velocity and attenuation data of sandstone samples to mineral composition and pore texture and vice versa. The data analysis presented furthermore emphasizes a workflow for how to predict changes in seismic parameters due to altered pore pressure and fluid composition for seismic to ultrasonic frequencies from laboratory data. As such, this study should provide a basis for feasibility studies to evaluate reservoir monitoring based on time lapse or 4D seismic data. A basic assumption of our approach is, however, that the reservoir conditions are equivalent on the core and seismic scale.

THE VISCOELASTIC MODEL

For our subsequent analysis, we shall use the effective viscoelastic medium model proposed by Jakobsen et al. (2003a, 2003b) with its extension to treat pressure effects as described in Jakobsen and Johansen (2005). Consider a homogeneous (isotropic or anisotropic) medium embedded with inclusions, divided into families $r = 1, 2, \ldots, N$ with the same shape/orientations. The inclusions can be solids, porous materials, or fluid-filled cavities (pores). While the theory is not limited to specific inclusion shapes, in practice they are usually considered of ellipsoidal shape represented by an aspect ratio $\alpha(r)$. The effective stiffness tensor $\mathbf{C}*$ of the medium is given by (Jakobsen et al., 2003a, 2003b)

$$\mathbf{C}* = \mathbf{C}^{(0)} + \mathbf{C}_1 : (\mathbf{I}_4 + \mathbf{C}_1^{-1} : \mathbf{C}_2)^{-1}, \quad (1)$$

$$\mathbf{C}_1 = \sum_{r=1}^{N} \mathbf{v}^{(r)} \mathbf{t}^{(r)}, \quad (2)$$

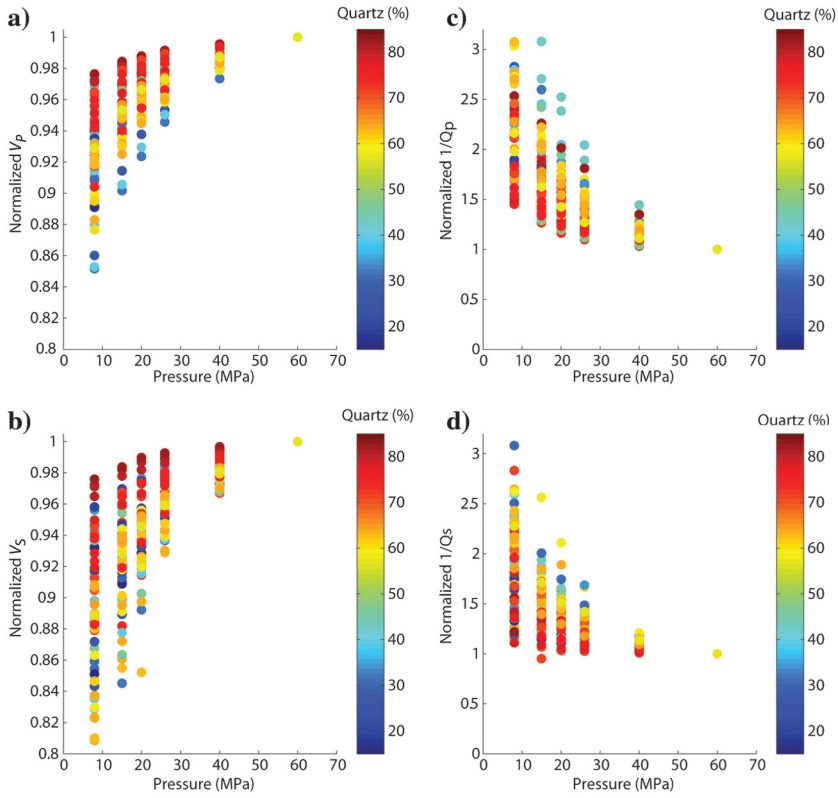

Figure 3. Normalized (a) P- and (b) S-wave velocity versus pressure for the 63 samples studied by Han et al. (2011a). Note that (clean) sandstones with a large quartz content are less stress sensitive than heterogeneous sandstones. Similarly, normalized attenuation of (c) P- and (d) S-wave versus pressure show an increase in stress sensitivity with increasing heterogeneities (decreasing quartz).

Table 1. Matrix of correlation coefficients for velocity and attenuation ratios (V_P/V_S, Qs/Qp) and petrophysical properties for the 63 sandstone samples analyzed (Han et al., 2011a). Note that the V_P/V_S ratio is strongly correlated with quartz content (mineralogy). In contrast, the Qs/Qp ratio is only slightly correlated to mineralogy.

Correlation matrix: for V_P/V_S, Qs/Qp ratios, and petrophysical properties

	V_P/V_S	Qs/Qp	Phi	Perm	Clay	Quartz	Feldspar	Other	Clay + Fd	Clay + Fd + other
V_P/V_S	1.00	0.23	0.10	−0.04	0.16	−0.74	0.54	0.43	0.58	0.66
Qs/Qp	0.23	1.00	0.10	−0.08	0.21	−0.12	−0.20	0.29	−0.09	0.08
Phi	0.10	0.10	1.00	0.53	−0.45	0.17	−0.15	−0.28	−0.35	−0.41
Perm	−0.04	−0.08	0.53	1.00	−0.39	0.13	0.01	−0.23	−0.18	−0.26
Clay	0.16	0.21	−0.45	−0.39	1.00	−0.25	−0.09	0.09	0.39	0.34
Quartz	−0.74	−0.12	0.17	0.13	−0.25	1.00	−0.78	−0.64	−0.84	−0.97
Feldspar	0.54	−0.20	−0.15	0.01	−0.09	−0.78	1.00	0.16	0.88	0.76
Other	0.43	0.29	−0.28	−0.23	0.09	−0.64	0.16	1.00	0.19	0.66
Clay + Fd	0.58	−0.09	−0.35	−0.18	0.39	−0.84	0.88	0.19	1.00	0.86
Clay + Fd + other	0.66	0.08	−0.41	−0.26	0.34	−0.97	0.76	0.66	0.86	1.00

$$\mathbf{C}_2 = \sum_{r=1}^{N}\sum_{s=1}^{N} \mathbf{v}^{(r)}\mathbf{t}^{(r)} : \mathbf{G}_d^{(rs)} : \mathbf{t}^{(s)}\mathbf{v}^{(s)}. \quad (3)$$

In these equations, $\mathbf{C}^{(0)}$ is the elastic stiffness tensor of the matrix material, $\mathbf{I}_4$ is the identity for the fourth-rank tensors, $v^{(r)}$ is the volume concentration of the rth family of inclusions, and $\mathbf{t}^{(r)}$ is the so-called T-matrix. The term $\mathbf{C}_2$ accounts for the two-point interactions between the rth and sth set of inclusions. The tensor $\mathbf{G}_d^{(rs)}$ is obtained by integrating the strain Green's function over an ellipsoid having the same symmetries (aspect ratio) as $p(s/r)$ $(\mathbf{x}-\mathbf{x}')$, which is the conditional probability of finding an inclusion of type s at point $\mathbf{x}'$ given that there is an inclusion of type r at point $\mathbf{x}$. The T-matrix for a single inclusion of type r is given by (Jakobsen et al., 2003a, 2003b)

$$\mathbf{t}^{(r)} = (\mathbf{C}^{(r)} - \mathbf{C}^{(0)}) : [\mathbf{I}_4 - \mathbf{G}^{(r)} : (\mathbf{C}^{(r)} - \mathbf{C}^{(0)})]^{-1}, \quad (4)$$

where $\mathbf{C}^{(r)}$ is the stiffness tensor of the inclusion and $\mathbf{G}^{(r)}$ is a fourth-rank tensor depending only on $\mathbf{C}^{(0)}$ and the shape/orientation of the rth inclusion type. In the case of dry cavities, we may set $\mathbf{C}^{(r)} = 0$.

For a fully fluid-saturated cavity that is allowed to exchange fluid mass with other cavities, the effective stiffness tensor is a complex-valued function of frequency. A detailed derivation of the fluid dependence can be found in Jakobsen et al. (2003b). In the following, we list the main expressions used in our modeling. In this case, the T-matrix is given by the T-matrix for a dry cavity and a term accounting for the fluid-flow effects (Jakobsen et al., 2003b):

$$\mathbf{t}^{(r)} = \mathbf{t}_d^{(r)} + \frac{\theta \mathbf{Z}^{(r)} + i\omega\tau k_f \mathbf{X}^{(r)}}{1 + i\omega\gamma^{(r)}\tau}, \quad (5)$$

where

$$\mathbf{X}^{(r)} = \mathbf{t}_d^{(r)} : \mathbf{S}^{(0)} : (\mathbf{I}_2 \otimes \mathbf{I}_2) : \mathbf{S}^{(0)} : \mathbf{t}_d^{(r)}, \quad (6)$$

$$\theta^{(r)} = \mathbf{t}_d^{(r)} : \mathbf{S}^{(0)} : (\mathbf{I}_2 \otimes \mathbf{I}_2) : \mathbf{S}^{(0)} : \left(\sum_{r=1}^{N_c} \frac{v^{(r)}\mathbf{t}_d^{(r)}}{1 + i\omega\gamma^{(r)}\tau} \right), \quad (7)$$

$$\theta = k_f \left\{ (1 - k_f \mathbf{S}^{(0)}_{uuvv}) \left(\sum_{r=1}^{N_c} \frac{v^{(r)}}{1 + i\omega\gamma^{(r)}\tau} \right) + k_f \left(\sum_{r=1}^{N_c} \frac{v^{(r)} (\mathbf{K}_d^{(r)})_{uuvv}}{1 + i\omega\gamma^{(r)}\tau} \right) - \frac{ik_u k_v \Gamma_{uv} k_f}{\eta_f \omega} \right\}^{-1}, \quad (8)$$

$$\gamma^{(r)} = 1 + k_f (\mathbf{K}_d^{(r)} - \mathbf{S}^{(0)})_{uuvv}, \quad (9)$$

$$\mathbf{K}_d^{(r)} = (\mathbf{I}_4 + \mathbf{G}^{(r)} : \mathbf{C}^{(0)})^{-1} : \mathbf{S}^{(0)}. \quad (10)$$

In these equations, $t_d^{(r)}$ is the T-matrix for the dry cavity of type r, $\mathbf{S}^{(0)} = (\mathbf{C}^{(0)})^{-1}$ is the compliance of the reference medium, k_f and η_f are the bulk modulus and viscosity of the fluid, ω is the angular frequency, τ is the relaxation-time constant, ku and kv are the components of the wavenumber vector, and Γ_{uv} is the component of the permeability tensor. The repeated subscripts u and v indicate summation over $u, v = 1, 2, 3$. The tensors $\mathbf{I}_2$ and $\mathbf{I}_4$ are the second- and fourth-rank identity tensor, respectively. The dyadic tensor product is denoted by the symbol $\otimes$.

The real-valued phase velocity and attenuation are obtained by inserting the tensor $\mathbf{C}^*$ of effective viscoelastic stiffness in the dispersion relation (Auld, 1990) and solving it through the eigenvalue/eigenvector method (Jakonsen et al., 2003b, Carcione, 2007). The phase velocity is the reciprocal of the slowness and in component form is given by (Carcione, 2007)

$$V_{\text{phase}} = \left[\text{Re}\left(\frac{1}{V} \right) \right]^{-1} \hat{I}. \quad (11)$$

The quality factor Q is defined as the ratio of the peak strain energy to the average loss energy density (Auld, 1990) and is defined by (Carcione, 2007)

$$Q = \frac{\text{Re}(V^2)}{\text{Im}(V^2)}. \quad (12)$$

It is worth noticing that the above model is Gassmann consistent, which means that modeled effects of pore fluid composition/saturation on elastic properties using Gassmann (1951) are equivalent to those from our model in the static limit when the pore space is connected (Jakobsen et al., 2003b).

The effects of pressure

To account for the pressure dependence, we shall use the evolution laws of microstructure proposed by Jakobsen and Johansen (2005) for a medium under finite deformation. These laws were derived assuming that the applied stress is triaxial with axes coinciding with the elastic symmetry of the medium, and the inclusions are ellipsoidal so that they deform into ellipsoids under uniform loading conditions.

The variation in volume $\partial v^{(r)}$ and aspect ratio $\partial\alpha^{(r)}$ of a cavity denoted by r (with $r = 1, 2, \ldots, N$) due to a small increment of effective strain ε under drained conditions is given by (Jakobsen and Johansen, 2005)

$$\frac{\partial v^{(r)}}{v^{(r)}} = \partial\varepsilon_{kk}^{(r)} - \sum_{s=0}^{N_c} v^{(s)} \partial\varepsilon_{kk}^{(s)}, \quad (13)$$

$$\frac{\partial v^{(r)}}{v^{(r)}} = \left[(K_{d*}^{(r)})_{kkpq} - \sum_{s=0}^{N_c} v^{(s)} (K_{d*}^{(s)})_{kkpq} \right] (\partial\langle\sigma\rangle_a^{(r)})_{pq}, \quad (14)$$

$$\frac{\partial\alpha^{(r)}}{\alpha^{(r)}} = \partial\varepsilon_{33}^{(r)} - \partial\varepsilon_{11}^{(r)}, \quad (15)$$

and

$$\frac{\partial\alpha^{(r)}}{\alpha^{(r)}} = [(K_{d*}^{(r)})_{33pq} - (K_{d*}^{(r)})_{11pq}](\partial\langle\sigma\rangle_a^{(r)})_{pq}. \quad (16)$$

In these equations, k, p, q represent summation ($k, p, q = 1, 2, 3$) and $K_{d*}^{(r)}$ is the effective dry K-tensor (Jakobsen and Johansen, 2005) given by

$$\mathbf{K}_{d*}^{(r)} = (\mathbf{I}_4 - \mathbf{G}^{(r)} : \mathbf{C}^{(0)})^{-1} (\mathbf{I}_4 + \mathbf{C}_{d1}^{-1} : \mathbf{C}_{d2})^{-1} : \mathbf{S}_d^*. \quad (17)$$

Here, the fourth-rank tensors $\mathbf{S}_d^* = (\mathbf{C}_\mathbf{d}^*)^{-1}$, $\mathbf{C}_{d1}$, and $\mathbf{C}_{d2}$, can be calculated with the T-matrix expression (equation 1) for dry inclusions. In addition, Jakobsen and Johansen (2005) give the apparent stress $\partial\langle\sigma\rangle_a^{(r)}$ as

$$\partial\langle\sigma\rangle_a^{(r)} = \partial\langle\sigma\rangle + \delta p_f \varsigma. \quad (18)$$

In equation 18, $\partial\langle\sigma\rangle$ is the effective stress and the second-rank tensor of apparent stress coefficient is

$$\varsigma^{(r)} = \mathbf{I}_2 - (\mathbf{K}_{d*}^{(r)})^{-1} \mathbf{S}^{(0)} \mathbf{I}_2. \quad (19)$$

Jakobsen et al. (2003a) show that the relaxation time constant depends on the scale and size of the pores, properties of the matrix mineral, permeability, and properties of the saturating fluid. Due to the challenge of measuring all these parameters, it is suggested that τ can be calibrated empirically for each rock and fluid type from pressure dependent velocity and/or attenuation measurements. For a particular pore type with a given aspect ratio, the characteristic frequency associated with the attenuation peak, is defined as (Jakobsen et al., 2003b)

$$f_c = \frac{1}{\gamma^{(r)} \tau}. \quad (20)$$

In this equation, $\gamma(r)$ depends on the aspect ratio, rock properties, and fluid modulus, as shown in equation 9. In the T-matrix formalism, τ- is a relaxation time constant that is scale dependent. The product between $\gamma^{(r)}$ and τ is the relaxation time period. Decreasing aspect ratio will increase $\gamma^{(r)}$ and hence would decrease characteristic frequency. Additionally, varying pore sizes would also affect the characteristic frequency through the τ- parameter. Because $\gamma^{(r)}$ accounts for the dependence on the fluid bulk modulus and τ can be calibrated empirically, we can set (Agersborg et al., 2009)

$$\tau = C_m \eta, \quad (21)$$

where C_m is an empirical constant accounting for all the parameters independent of the saturating fluid and η is the fluid viscosity. In the existence of velocity and/or attenuation measurements for a rock with a particular fluid, equation 21 can be used to estimate the relaxation time constant for other fluids as (Agersborg et al., 2009)

$$\tau_{\text{fluid2}} = \tau_{\text{fluid1}} \frac{\eta_{\text{fluid2}}}{\eta_{\text{fluid1}}}. \quad (22)$$

MODELING AND DATA ANALYSIS

We now use the above-described viscoelastic theory to analyze the data of Han et al. (2011a, 2011b). The pores are considered of ellipsoidal shapes, and they are in communication as they can exchange fluid-mass accounting for global and local fluid-flow effects as described by Jakobsen and Chapman (2009). Furthermore, the aspect ratios of the pores alter with altered pressure as given by Jakobsen and Johansen (2005). This provides the necessary framework for modeling P-wave and S-wave velocity and attenuation including frequency and pressure dependencies.

The approach is similar to the Xu and White (1995) sand-clay model, which divides the pore space into stiff (quartz-related) and compliant (clay-related) pores. Essentially, Xu and White (1995) associate the clay minerals with flatter pores (more compliant) rather than with the quartz-related pores. In our model, we also associate the quartz content with the stiff pores. But the compliant pores are associated with all the other secondary minerals different from quartz, such as clay minerals, feldspars, micas, etc. We use the T-matrix formulation to insert solid and fluid inclusions in a homogeneous matrix of quartz. The solid inclusions are not in communication and represent the secondary minerals that are incorporated as a constituent of the matrix. The quartz-related pores are approximated by fairly stiff ellipsoids ($\alpha_{(1)} \sim 0.15$), and they account for most of the porosity. The nonquartz-associated (compliant) porosity is made up of relatively flat pores ($\alpha_{(2)} \sim 0.05$). We also include a distribution of small-aspect-ratio pores (crack-like) sufficiently wide to mimic the nonlinear behavior of the velocity-pressure relationship usually observed in experimental data. For simplicity, we shall consider all the pore inclusions to be randomly oriented so that the medium occurs elastically isotropic. Similarly to Xu and White (1995), we make the key assumption that the relative pore volume of compliant pores is proportional to the content of minerals different from quartz.

For illustration, let us consider a quartz matrix with spherical inclusions of isotropic clay as the only secondary mineral. The total porosity is $\Phi = 0.2$, and the clay content is $\text{Vc} = 0.1$. The aspect ratio of quartz-related pores is $\alpha_{(1)} = 0.15$, and the compliant pore shapes are defined by $\alpha_{(2)} = 0.05$ at a given pressure state. In our modeling, we assume an initial effective pressure of 1 MPa. A small amount of cracklike inclusions is also included and described by a beta distribution function of aspect ratios as was done by Agersborg et al. (2008) and defined in Appendix A. The inclusions are randomly oriented, so the medium is isotropic. We consider low permeability (50 mD) to emphasize the effects of squirt flow. Following Jakobsen et al. (2003b), we use $\tau = 1e^{-7}$ for the relaxation time constant and 10^{-3} Pa s for the viscosity of water (Pointer et al., 2000).

Figure 4 shows modeled P and S velocities and attenuations for a range of frequencies at initial pressure. The presence of pores of various shape and random orientation produces local fluid-pressure gradients, and thereby fluid-flow, which causes velocity dispersion and attenuation. The attenuation spectra show two attenuation peaks related to wave-induced fluid flow among the different pore systems. The peak at high frequencies depends on the clay-related pores $\alpha_{(2)}$ and clay content Vc, while the peak at low frequencies depends on the crack distribution function defined by $\alpha_{(3)}$ and the crack density ε (Appendix A). Increasing clay content would produce an overall decrease in velocity and a significant increase in the maximum attenuation value of the high-frequency peak (not shown in Figure 4). Increasing the volume fraction of cracklike pores (crack density) causes a decrease in velocity and an increase in attenuation and dispersion at low frequencies (Figure 4). Of crucial importance is the relaxation time constant because it controls the frequency range over which the dispersion occurs. The effect of

reducing the relaxation time parameter is to move the attenuation peaks toward lower frequencies while the dispersion increases.

Observed and modeled stress sensitivity

For the modeling, we divide the mineralogy into two groups: stiff and compliant pore shape constituents. In the first group, we include minerals associated with stiff pore shapes, which, in our case, is defined by quartz only. The second group contains clays, feldspars, calcite, and other occasional minerals. This allows us to model stress dependence in terms of the volume fractions of the minerals associated with stiff or soft pore shapes.

To analyze pressure sensitivity of the velocity and attenuation data of Han et al. (2011a) to our modeled data, comparisons are normalized using values at initial pressure. This restricts our analysis to study observed and modeled trends of velocity and attenuation versus pressure. We now define an "average" sandstone with matrix composed by 90% of quartz and 10% kaolinite, porosity $\Phi = 0.15$, quartz-related pores of aspect ratio $\alpha_{(1)} = 0.15$, clay-related pores by $\alpha_{(2)} = 0.025$, and permeability $k = 100$ mD. We include a set of randomly oriented cracks, which has a very small contribution to the total porosity, but they play a key role in the pressure sensitivity of velocity and attenuation (Nur and Simmons, 1969; Sayers, 1988; Mavko et al., 1995). The crack distribution function is defined by the following parameters: $\delta = 0.8$, $\alpha_m = 0.001$, and $\mu = 0.01$, where the terminology is defined in Appendix A. Crack density is the dominant parameter controlling pressure sensitivity, and it varies between $\varepsilon = 0.05$ and 0.3. Following Jakobsen et al. (2003b) and Agersborg et al. (2007), we first use a constant relaxation time $\tau = 10e^{-7}$ for the three pore types in the model.

Figure 5 shows modeled and observed data, in which the curves denote crack densities varying from $\varepsilon = 0.05$ to $\varepsilon = 0.30$. The higher the crack density is, the higher is the pressure sensitivity of all the modeled data. The velocity behavior of the more dirty sands (quartz content less than 60%) is not reproduced by the model. S-wave velocity variations with pressure are somewhat better reproduced than P-wave data. The model fails to reproduce P- and S-wave attenuation data. In Figure 6, modeled velocities and attenuations as function of frequency at initial pressure are shown for the various crack densities. The two attenuation peaks at distinctive characteristic frequencies of approximately 50 and 800 kHz are associated with cracks and mesopores, respectively. P-wave attenuation is modeled slightly larger than S-wave attenuation. The ultrasonic data were obtained at 1.0 MHz for the P-wave and at 0.7 MHz for the S-wave. Consequently, this indicates that squirt flow related to mesopores has a much stronger effect on the observed dispersion and attenuation than the cracks. The same can be said for Figure 4.

The results above were obtained using an equal relaxation time constant (τ) for all the three pore types considered. Previous studies have suggested that the relaxation time constant depends on the scale of the pores (Jakobsen et al., 2003b; Agersborg et al., 2007), and so that smaller pores imply smaller relaxation time constant. In the next modeling, we assume a relaxation time constant (τ) of the cracks to be one order of magnitude smaller than for the mesopores. In Figures 7 and 8, we use the relaxation time constants $\tau = 10e^{-8}$ for cracks and $\tau = 10e^{-7}$ for mesopores. The effect of reducing the relaxation time constant for cracks moves the corresponding attenuation peak to higher frequencies, and, consequently, the characteristic frequencies of meso- and micropores converge and the two attenuation peaks superimpose to produce increased attenuation. The curves show that the modeled velocity and attenuation data now better resemble the measured data; i.e., the signatures of the P- and S-waves versus pressure are improved. The results indicate that pores of different scales are likely to be defined by different relaxation time constants in the viscoelastic modeling scheme.

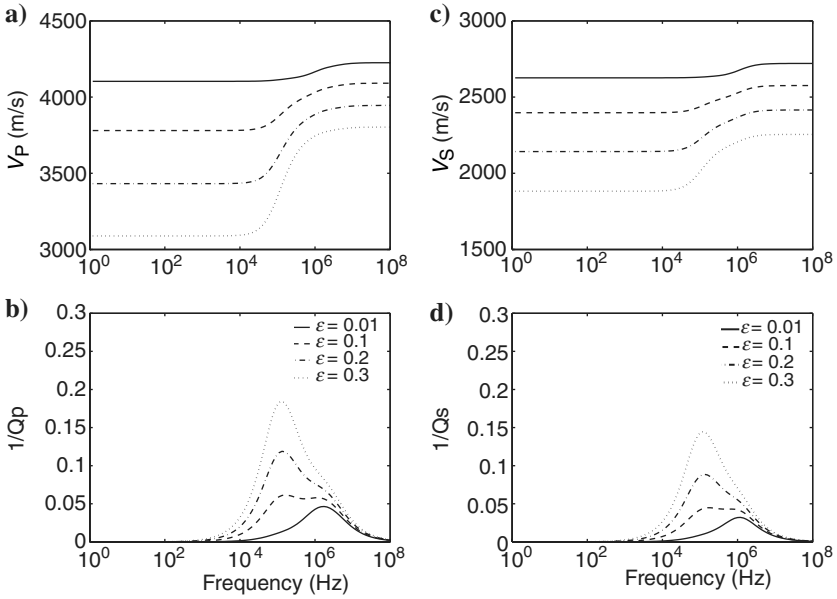

Figure 4. P-wave (a) velocity and (b) attenuation spectra and S-wave (c) velocity and (d) attenuation spectra, for a sandstone with $\Phi = 0.2$ and kaolinite content of Vc = 0.1. Three kinds of pores were included: stiff quartz-related pores, compliant clay-related pores, and cracks. The effective pressure is 1 MPa, and a range of frequencies is shown. Note that increasing the crack density from $\varepsilon = 0.01$ to $\varepsilon = 0.3$ decreases the overall velocity and increases the attenuation peak value at low frequency. The relaxation time constant is equal for all the pores $\tau = 10^{-7}$.

Modeling clean versus heterogeneous sandstones

In the previous section, we focused on how the pore's texture and pore scale affect pressure signatures of velocity and attenuation. In the following section, we select a subset of 10 samples to study velocity and attenuation data in which the mineral composition varies from almost pure quartz to highly heterogeneous sandstone. We consider three clean sandstones with more than 80% of quartz and approximately 5% of K-feldspar on average. The other seven samples have between 57% and 68% of quartz, with the remaining minerals constituted by variable amounts of clay and feldspars. By trial and error, we defined two elastic end members as defined in Figure 9.

The model is constructed considering a quartz matrix containing a volume fraction V_{sec} of spherical inclusions of a secondary mineral with elastic properties of gulf clays (Mavko et al.,

2009). The values used were $V_P = 3810$ m/s, $V_S = 1880$ m/s, and density $\rho = 2.55$ g/cc. The parameters describing the pore texture and pore size were then defined from the volume fractions of quartz $(1 - V_{sec})$ and secondary mineral (V_{sec}) following the procedures from the previous section. The remaining model parameters are given in Table 2. Figure 9 reveals that the model fairly well spans the velocity and attenuation data for all mineral compositions. Because velocity variation with pressure is mainly controlled by the amount (crack density) and closure of cracks, a small amount of cracks ($\varepsilon = 0.02$) was included in the clean sandstone model at the initial pressure state to reproduce the data trends. Again, the relaxation time constant τ of cracks was set one order of magnitude larger than for the mesopores. Relating the pore fluid relaxation time constant to pore size was important to calibrate the modeled and measured attenuation data. For the heterogeneous sandstones, the volume fraction of secondary minerals was set to $V_{sec} = 0.15$. In addition to the corresponding pore texture, a crack density $\varepsilon = 0.2$ was added to adapt the significant pressure dependence seen in the

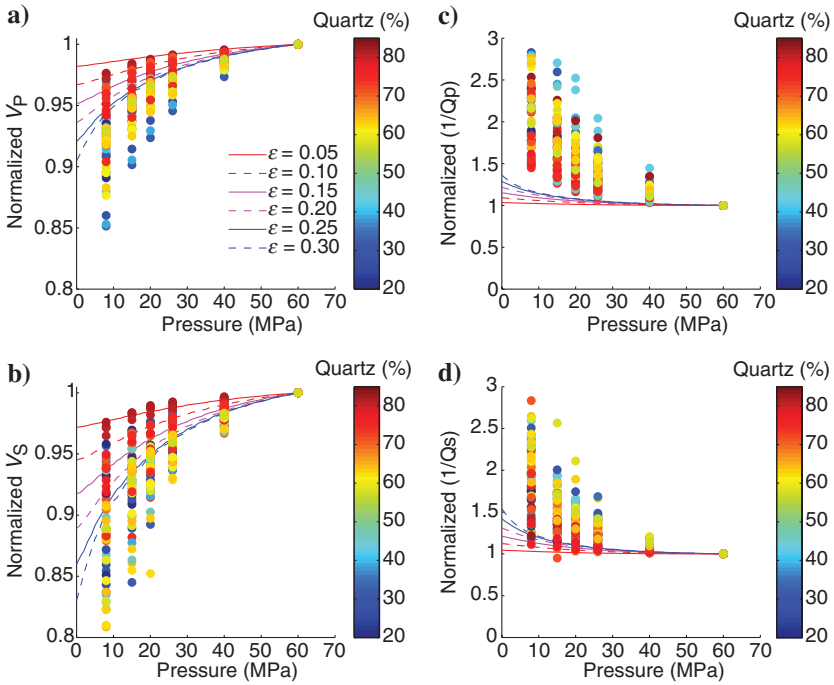

Figure 5. The modeled and experimental data presented as normalized (a) P- and (b) S-wave velocity versus pressure and normalized attenuation of (c) P- and (d) S-wave versus pressure. The 63 samples studied by Han et al. (2011a) are included. The model consist of a quartz matrix with spherical inclusion of kaolinite (10%), with porosity of $\Phi = 0.15$, aspect ratios of pores $\alpha_{(1)} = 0.15$, $\alpha_{(2)} = 0.025$, permeability $k = 100$ mD, and a certain amount of cracks given by the crack density. The different model lines are results for crack density from $\varepsilon = 0.05$ to 0.30. The relaxation time constant is equal for all the pore types in the modeling ($\tau = 10e^{-7}$). Increasing crack density increases the pressure sensitivity of the model. Velocities are partially well reproduced, but attenuation measurements are not matched.

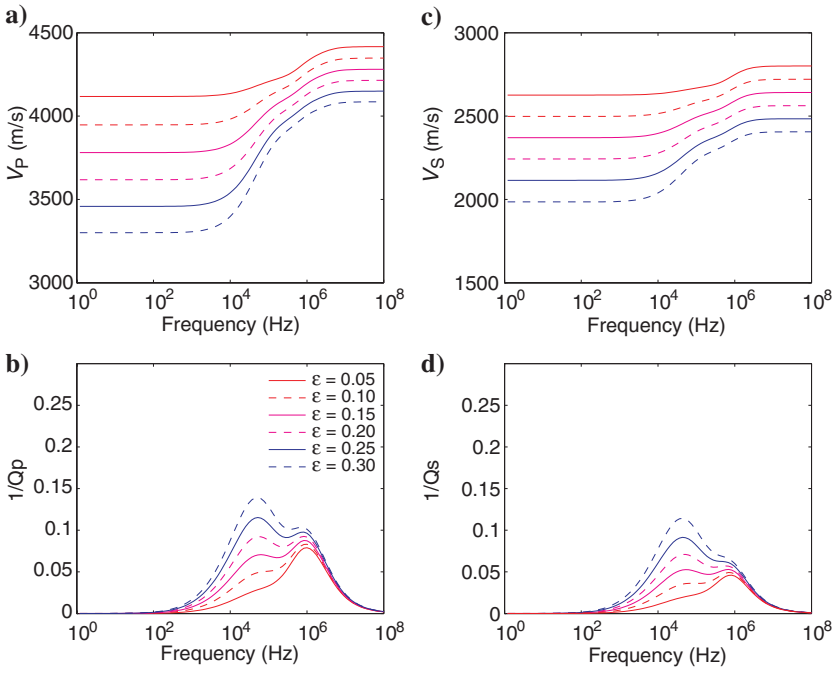

Figure 6. P-wave (a) velocity and (b) attenuation spectra, and S-wave (c) velocity and (d) attenuation spectra for a sandstone with $\Phi = 0.15$ and kaolinite content of Vc = 0.1. Three kinds of pores were included: stiff quartz-related pores ($\alpha_{(1)} = 0.15$), compliant clay-related pores ($\alpha_{(2)} = 0.025$), and cracks. The effective pressure is 1 MPa. The relaxation time constant is equal for all the pores $\tau = 10^{-7}$. Note that the two attenuation peaks have maximums at 0.05 (cracks) and 0.8 MHz (clay content). Thus, at the frequencies used in the measurements, 1 MHz for P-waves and 0.8 for S-waves, the crack porosity has minimum contribution to the total attenuation in this modeling.

data. Figure 10 shows P and S velocities and attenuations versus frequency for the clean and heterogeneous sandstone model at 1 MPa effective pressure. The measured P- and S-wave data are also indicated at frequency 1 and 0.7 MHz, respectively. The modeling results reveal that the (compliant) heterogeneous sandstone has lower seismic velocities and larger attenuation and dispersion than the (stiff) clean sandstones.

The fluid effect

In the following, we model clean and heterogeneous sandstones with different saturating fluids. We used equation 21 and the relaxation time constants (τ) determined empirically for brine saturation (see Table 2) to calculate the τ-constant for the case of oil and gas saturation. The fluid properties are given in Table 3. Figure 11 shows the velocity modeled dispersion and attenuation patterns

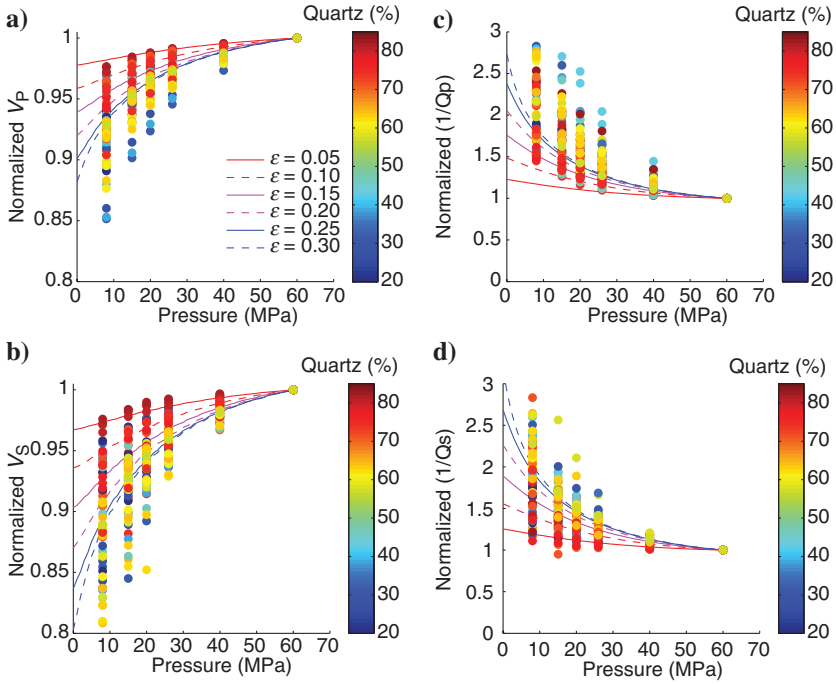

Figure 7. The modeled and experimental data presented as normalized (a) P- and (b) S-wave velocity versus pressure and normalized attenuation of (c) P- and (d) S-wave versus pressure. The 63 samples studied by Han et al. (2011a) are included. The model consist of a quartz matrix with spherical inclusion of kaolinite (10%), porosity of $\Phi = 0.15$, aspect ratios of pores $\alpha_{(1)} = 0.15$, $\alpha_{(2)} = 0.025$, permeability $k = 100$ mD, and various amount of cracks given by the crack density. The different model lines are results for crack density from $\varepsilon = 0.05$ to 0.30. The relaxation time is equal for quartz and clay associated pores ($\tau = 10e^{-7}$) and one order of magnitude smaller for cracks ($\tau = 10e^{-8}$). The velocities and attenuation observation are much better reproduced than in the model with constant relaxation time (Figure 5).

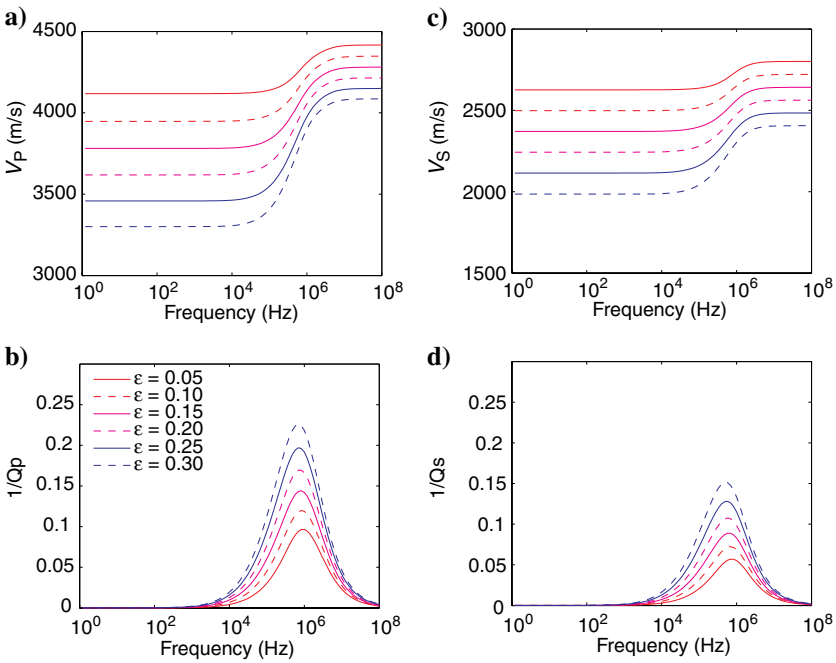

Figure 8. P-wave (a) velocity and (b) attenuation spectra and S-wave (c) velocity and (d) attenuation spectra for a sandstone with $\Phi = 0.15$, kaolinite content of Vc = 0.1, and three kinds of pores: stiff quartz-related pores ($\alpha_{(1)} = 0.15$), compliant clay-related pores ($\alpha_{(2)} = 0.025$), and cracks. The effective pressure is 1 MPa. The relaxation time constant is equal for quartz and clay associated pores ($\tau = 10e^{-7}$) and one order of magnitude smaller for cracks ($\tau = 10e^{-8}$). The attenuation peaks of cracks and clay have similar characteristic frequencies and increased the overall attenuation and dispersion in the model.

for the clean sandstone saturated with various fluids: brine, oil, or gas. Equation 22 shows that once a τ-constant is estimated empirically for a particular fluid, the corresponding τ for other saturating fluids is controlled by the viscosity ratio between the new and the initial fluid. Because τ and the characteristic frequency f_c are inversely related, we observe that an increase in fluid viscosity moves the attenuation peak to low frequencies. In the cases of brine, oil, and gas saturation, with viscosity values such as $\eta_{oil} > \eta_{brine} > \eta_{gas}$, the attenuation peaks are organized along the frequency axis with the peak of the most viscous fluid occurring at lower frequencies than the less viscous fluids. Thus, when the pore fluid is oil, the characteristic frequency is lower than when the fluid is brine or gas ($f_{c-oil} < f_{c-brine} < f_{c-gas}$). This indicates that increasing the viscosity of the pore fluid moves the dispersion effects to occur at lower seismic frequencies. This agrees well with the concept of fluid mobility, defined as the ratio between permeability and viscosity by Batzle et al. (2006). Overall, the maximum P- and S-wave attenuation values are larger for brine than for the other two fluids. Gas saturation seems to cause the smallest attenuation peak with dominant velocity dispersion effects occurring only at frequencies above 1 MHz.

Figure 12 shows the dispersion and attenuation spectra for the heterogeneous sandstone model described in Table 2 with various saturating fluids. Similarly to the clean sandstone model, the characteristic frequency of each fluid-case organizes along the frequency axis according to their relative pore fluid viscosities, with the most viscous fluid (oil) having the least f_c and the less viscous fluid (gas) causing the greatest f_c. In contrast to the clean sandstone model, the maximum attenuation value for P-waves occurs with gas as the pore fluid. The heterogeneous sandstone model produces larger attenuation than the clean sandstone model. Also, it is worth noticing that the fluid causing the largest attenuation depends on the pore texture and the corresponding relaxation time constant. Thus, it also varies with the frequency of measurement. For instance, in the heterogeneous sandstone model (Figure 12), we observe that brine is the most attenuating fluid at ultrasonic (10^6 Hz) frequencies, whereas oil shows the largest attenuation at sonic frequencies (10^4 Hz).

DISCUSSION

Previous studies of water-saturated sandstones (Tosaya and Nur, 1982; Castagna et al., 1985; Han et al., 1986; Klimentos and McCann, 1990) found that P- and S-wave velocities depend upon porosity and clay content. Hence, it was suggested that the V_P/V_S ratio also depends on porosity and clay content (Han et al., 1986). However, in the samples used for this study, V_P shows a strong dependence on porosity, with a correlation coefficient of $r = 0.78$,

Table 2. Parameters of the model for clean and heterogeneous sandstones presented in Figures 9 and 10. The parameters are as follows: porosity, volume of secondary minerals, aspect ratio, and relaxation times of (1) stiff and (2) compliant pores, cracks relaxation time, crack density, and permeability in mD.

Clean and heterogeneous sands — Model parameters									
	Phi	V_{sec}	α_1	α_2	τ_1	τ_2	τ_{cracks}	ε	K
Clean sst	0.13	0.03	0.15	0.03	$4*10^{-7}$	$4*10^{-7}$	$4*10^{-8}$	0.02	10
Heterogeneous sst	0.13	0.15	0.15	0.03	$4*10^{-7}$	$4*10^{-7}$	$4*10^{-8}$	0.20	10

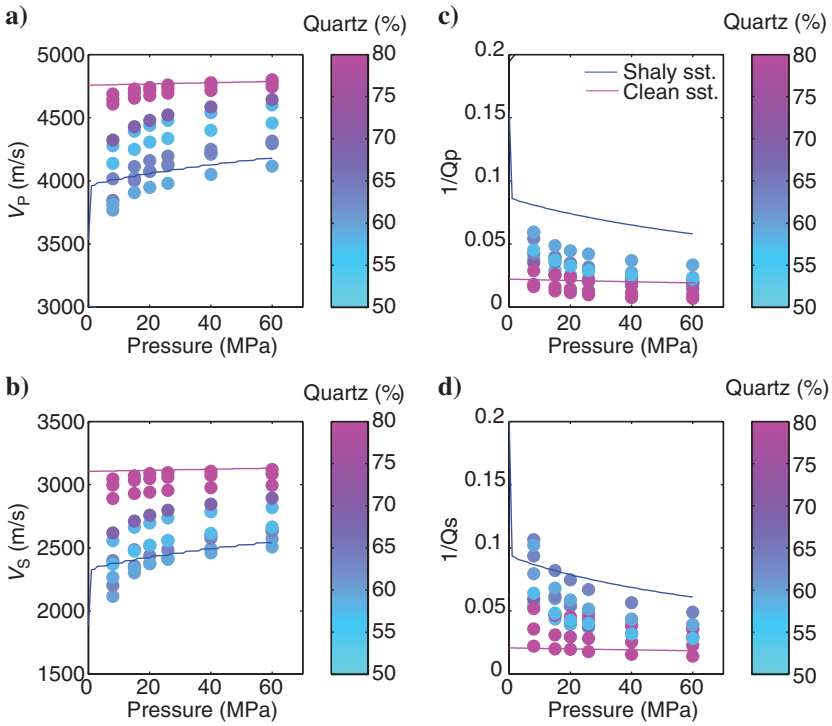

Figure 9. Ten samples studied in laboratory with variable quartz content, along with two modeling results (solid lines). (a) P- and (b) S-wave velocity versus pressure and attenuation of (c) P- and (d) S-wave versus pressure are shown. The model is constructed as a quartz matrix with inclusion of a secondary mineral comprised of clays. The magenta line is a clean sand with $\Phi = 0.13$, volume of secondary mineral $V_{sec} = 0.03$, $\alpha_{(1)} = 0.15$, $\alpha_{(2)} = 0.03$, $\tau_{(1)} = \tau_{(2)} = 4 * 10e^{-7}$, $\tau_{(3)} = 4 * 10e^{-8}$, crack density $\varepsilon = 0.02$, and $k = 10$ mD. The blue line is a heterogeneous sandstone with $\Phi = 0.13$, volume concentration of secondary mineral $V_{sec} = 0.15$ crack density $\varepsilon = 0.2$, $k = 10$ mD, and all the others parameters equal to the clean sand. It is noticeable that the viscoelastic model for heterogeneous sandstones can reproduce most of the variability observed in the data.

but it does not show a clear dependence on mineralogy. By contrast, the S-wave velocity correlates with porosity ($r = 0.61$) and also weakly with the quartz content ($r = 0.42$). Thus, the V_P/V_S ratio shows the highest correlation coefficient with quartz content ($r = 0.74$); see Table 1. This suggests that the abundance/lack of quartz in sandstone would be a critical petrophysical parameter in controlling the V_P/V_S ratio rather than the content of secondary minerals such as clay, feldspars, and other associated minerals. This may be due to the high shear modulus of quartz compared with most other minerals, or it may be due to the presence of quartz cement.

Because the V_P/V_S ratio relates to the degree of rock consolidation (Mavko et al., 2009), it is not surprising that the content of quartz also seems to correlate with its sensitivity to altered effective pressure as revealed by the samples shown in Figure 3. Moreover, quartz is the most stable mineral in sedimentary rocks followed by feldspar and clays, and its abundance/lack indicates the compositional maturity of sandstones (Tucker, 1991). Therefore, the pressure sensitivity of a sandstone reservoir may be predicted from its compositional maturity. The more mature sandstones are, i.e., homogeneous composition largely dominated by quartz and some feldspar (clean sands), the less pressure sensitive they tend to be. Conversely, immature sandstones with heterogeneous composition containing many labile grains of feldspars and less quartz dominated (shaly sands) would cause larger pressure sensitivity. The reason for this can be that the abundance of secondary minerals provides softer and more diverse grain contacts. This relationship should be important to consider for the interpretation of time-lapse seismic data. The sensitivity of the seismic parameters of rocks to changes in effective pressure is normally associated with the closure of cracks and stiffening of grain contacts (Nur and Simmons, 1969; Nur, 1971; Sayers, 1988; Mavko et al., 1995). Therefore, the dependence on compositional maturity observed in these samples may not always be a dominant factor. Often, this could be masked by natural cracks or cracks formed during the extraction and manipulation of core samples.

Agersborg et al. (2007) find that the microstructural model of Chapman (Chapman et al., 2002; Chapman, 2003) is a special case of the *T*-matrix approach of Jakobsen et al. (2003a, 2003b). They argue that the relaxation time τ is a constant depending on the scale of the pores. In their model containing (fractures) macro- and micropores, they assume that the relaxation constant of the microporosity, i.e., equant pores and cracks, could be found by calibration of velocity and attenuation measurements in saturated core plugs. Afterward, they calculated the τ of fractures, i.e., at a macroscale, through a scale ratio between the micropores and the fractures (Agersborg et al., 2007). Similarly, if we assume that the cracks in our model are much smaller (along the long axis) than the equant and ellipsoidal pores, we can assume that those cracks have much smaller relaxation time constant. Our calibration to the core plug measurements showed that this range in relaxation times is necessary to model the range of attenuation values. Moreover, it is of critical importance to determine the appropriate relaxation time constants for the different pore sizes to be able to model the dispersion signature of the rocks, i.e., the transition from low- to high-frequency behavior. Further empirical calibration of relaxation time constants could be achieved with velocity and attenuation measurements on various frequency ranges. Unfortunately, these sorts of experimental data are rarely available.

Table 3. Fluid parameters used in the modeling (Batzle and Wang, 1992), calculated for temperature 80°C and pore pressure 40 MPa.

	Brine	Oil	Gas
V_P (m/s)	1554.0	1424.3	688.7
Density (kg/m^3)	989.1	854.2	206.5
Viscosity (cP)	1.0	6.4	0.029

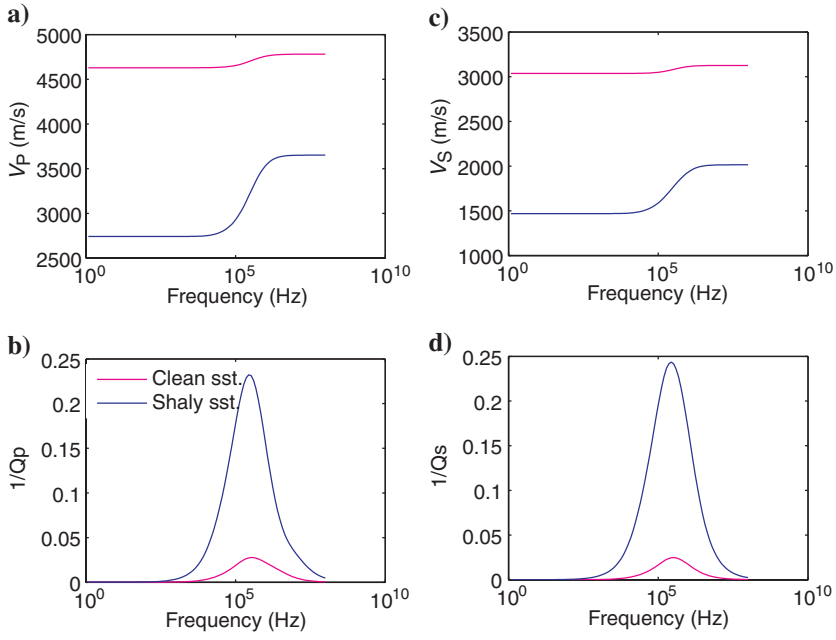

Figure 10. P-wave (a) velocity and (b) attenuation spectra, and S-wave (c) velocity and (d) attenuation spectra for the clean (magenta) and heterogeneous sandstones described in Figure 9. Note that heterogeneous sandstone is much more dispersive and attenuating than the clean sand model.

The relatively large number of adjustable parameters in the model makes the calibration challenging and interpretation nonunique. One way of reducing this ambiguity is by collecting more measurements to constrain the parameters' calibration. Measurements of velocity and attenuation with varying pressure and frequency, microscope images of pore structure, porosity, permeability, composition, and sedimentary facies would constrain the range of parameter values and increase confidence in the interpretation. In a field case, a combination of such a laboratory data set along with a viscoelastic modeling of the kind proposed in this paper would give an optimum foundation to characterize the 4D fluid and pressure response expected at seismic frequencies. If such a modeling shows that viscoelastic effect are not an issue for low frequencies, the properties of the dry rock estimated from viscoelastic modeling at high frequency can be used in conjunction with the Gassmann equation (Gassmann, 1951) to predict fluid time-lapse effects for low frequencies.

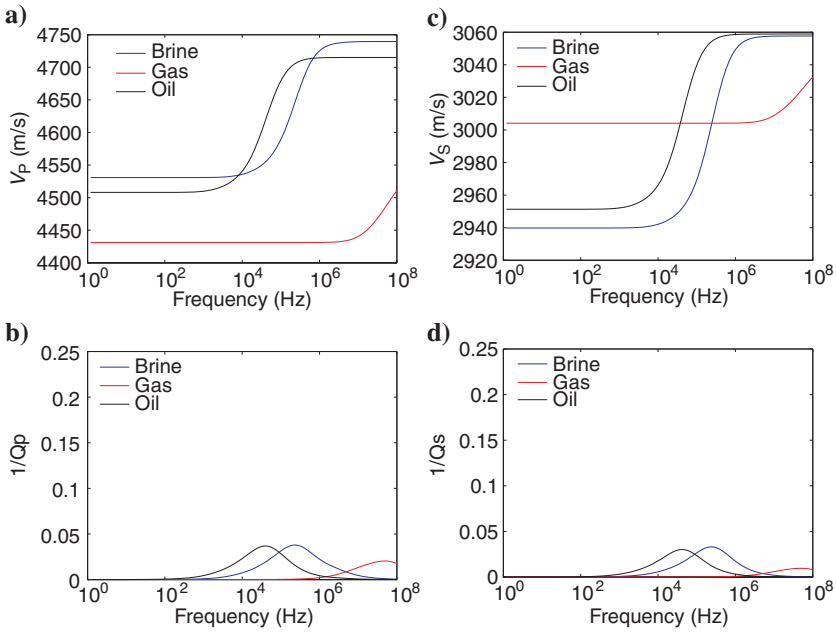

Figure 11. P-wave (a) velocity and (b) attenuation spectra, and S-wave (c) velocity and (d) attenuation spectra for a clean sandstone model saturated by different fluids. The brine, oil, and gas cases are represented by blue, black, and red lines. Increasing the viscosity of the fluid produces a shift of the attenuation peak toward low frequencies.

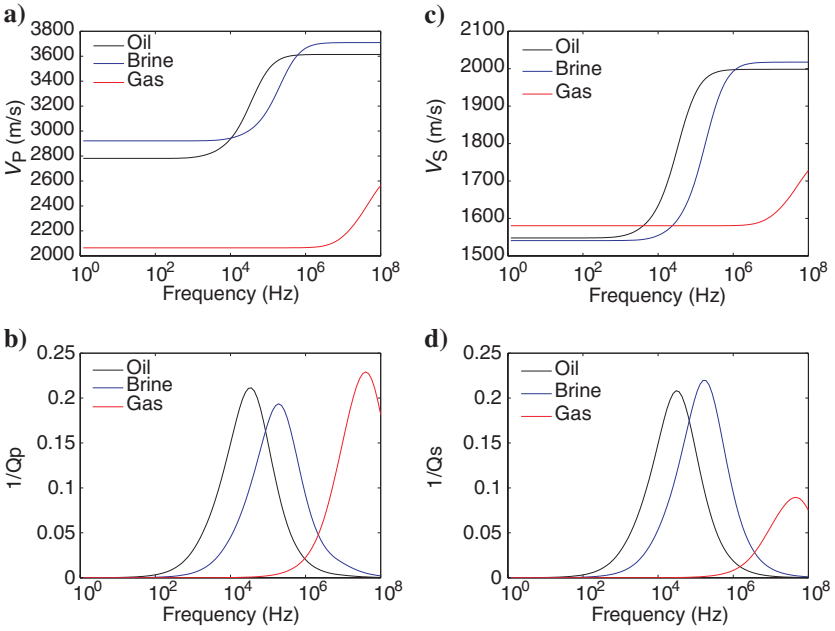

Figure 12. P-wave (a) velocity and (b) attenuation spectra, and S-wave (c) velocity and (d) attenuation spectra for a heterogeneous sandstone model saturated by different fluids. The brine, oil, and gas cases are represented by blue, black, and red lines. Note that the attenuation is significantly larger than for the clean sandstone model (compare with Figure 11). Increasing the viscosity of the fluid produces a shift of the attenuation peak toward low frequencies.

The viscoelastic modeling of clean and heterogeneous sandstones showed that the pore structure, in association with the relaxation time constant and fluid viscosity, determines the dispersion and attenuation spectra of siliciclastic rocks. Our modeling study has shown that for seismic time-lapse studies to reveal calibrated changes in pore fluid composition and pressure it is crucial to have information about compositional maturity and expected pore texture. Our approach shows how this information can be obtained from the dispersion and pressure signatures observed in the laboratory for various reservoir samples.

CONCLUSIONS

We have used a viscoelastic rock-physics model to evaluate the dispersion and pressure signatures measured for a suite of siliciclastic rock samples. Fundamental in our approach is to assign a pore texture model dependent on lithological composition and size of the pores. Our aim was to consistently model the observed velocity and attenuation data. We observed that the pressure dependency of velocity and attenuation of sandstones increased with the concentration of secondary minerals such as clays and feldspar (other than quartz). This means that clean sandstones tend to be stiffer than heterogeneous (shaly) sandstones. The model accounted for this differential pressure sensitivity by associating pores of different compliance nature to the corresponding mineralogy. The calibration to normalized data showed that pores of different scales such as mesopores and cracks require significantly different squirt-flow relaxation time constants. The relaxation constant associated with cracks can be one order of magnitude smaller than that of mesopores. We found that associating pores of different scales to different squirt-flow relaxation times improved the predictive power of the model allowing to reproduce

velocity and attenuation pressure dependencies. It is necessary to include a small amount of cracks to reproduce the observed nonlinear behavior of velocity versus pressure in heterogeneous and clean sandstones. We believe that complexities in rock composition such as the presence of minerals different from quartz tend to soften sandstones by adding diverse and softer grain contacts.

ACKNOWLEDGMENTS

This study has been partially funded by the Norwegian Research Council through the Petromaks Program. Moyano also would like to thank Statoil for granting a leave to pursue doctoral studies. We want to thank the reviewers for their comments, which helped to improve the paper.

APPENDIX A

CRACK DISTRIBUTION FUNCTION

To reproduce the variations of velocity with increasing pressure observed in laboratory studies of rock samples, it is necessary to include a continuous distribution of low-aspect-ratio inclusions (cracks) in the model. Following Agersborg et al. (2008) and Tod (2001), the crack distribution in the model can be expressed as the product between the total crack density and a generalized beta probability function. The crack density distribution is then written as

$$\varepsilon = \varepsilon_0 F_\beta(\alpha, \bar{\alpha}, \delta, u), \tag{A-1}$$

where ε_0 is the total crack density and $F_\beta(\alpha)$ is the generalized beta probability function described as (Tod, 2001)

$$F_\beta(\alpha) = \frac{1}{u}\frac{\Gamma(p+q)}{\Gamma(p)\Gamma(q)}\left(1-\frac{\alpha}{u}\right)^{q-1}\left(\frac{\alpha}{u}\right)^{p-1}, \tag{A-2}$$

with

$$p = \frac{u-\bar{\alpha}-\bar{\alpha}\delta^2}{u\delta^2}, \tag{A-3}$$

$$q = \frac{u-\bar{\alpha}}{\bar{\alpha}}p. \tag{A-4}$$

In these equations, Γ is the gamma function, α is the aspect ratio of inclusions, $\bar{\alpha}$ is the mean aspect ratio, δ is a parameter controlling the shape of the distribution, and u is the largest aspect ratio in the distribution.

REFERENCES

Agersborg, R., M. Jakobsen, B. O. Ruud, and T. A. Johansen, 2007, Effects of pore fluid pressure on the seismic response of a fractured carbonate reservoir: Studia Geophysica et Geodaetica, **51**, 89–118, doi: 10.1007/s11200-007-0005-8.

Agersborg, R., T. A. Johansen, and M. Jakobsen, 2009, Velocity variations in carbonate rocks due to dual porosity and wave-induced fluid flow: Geophysical Prospecting, **57**, 81–98, doi: 10.1111/j.1365-2478.2008.00733.x.

Agersborg, R., T. A. Johansen, M. Jakobsen, J. Sothcott, and A. Best, 2008, Effects of fluids and dual-pore systems on pressure-dependent velocities and attenuations in carbonates: Geophysics, **73**, no. 5, N35–N47, doi: 10.1190/1.2969774.

Auld, B. A., 1990, Acoustic fields and waves in solids: Krieger Publishing Company.

Batzle, M., D. H. Han, and R. Hofmann, 2006, Fluid mobility and frequency-dependent velocity — Direct measurements: Geophysics, **71**, no. 1, N1–N9, doi: 10.1190/1.2159053.

Batzle, M., and Z. J. Wang, 1992, Seismic properties of pore fluids: Geophysics, **57**, 1396–1408, doi: 10.1190/1.1443207.

Blangy, J. P., 1992, Integrated seismic lithologic interpretation: The petrophysical basis: Ph.D. thesis, Stanford University.

Carcione, J., 2007, Wave fields in real media: Wave propagation in anisotropic, anelastic, porous and electromagnetic media: Elsevier Science.

Castagna, J. P., M. L. Batzle, and R. L. Eastwood, 1985, Relationships between compressional-wave and shear-wave velocities in clastic silicate rocks: Geophysics, **50**, 571–581, doi: 10.1190/1.1441933.

Chapman, M., 2003, Frequency-dependent anisotropy due to meso-scale fractures in the presence of equant porosity: Geophysical Prospecting, **51**, 369–379, doi: 10.1046/j.1365-2478.2003.00384.x.

Chapman, M., S. V. Zatsepin, and S. Crampin, 2002, Derivation of a microstructural poroelastic model: Geophysical Journal International, **151**, 427–451, doi: 10.1046/j.1365-246X.2002.01769.x.

Cleary, M. P., 1977, Fundamental solutions for a fluid-saturated porous solid: International Journal of Solids and Structures, **13**, 785–806, doi: 10.1016/0020-7683(77)90065-8.

Dvorkin, J., and A. Nur, 1996, Elasticity of high-porosity sandstones: Theory for two North Sea data sets: Geophysics, **61**, 1363–1370, doi: 10.1190/1.1444059.

Gassmann, F., 1951, Elastic waves through a packing of spheres: Geophysics, **16**, 673–685, doi: 10.1190/1.1437718.

Gueguen, Y., M. Adelinet, A. Ougier-Simonin, J. Fortin, and A. Schubnel, 2011, How cracks modify permeability and introduce velocity dispersion: Examples of glass and basalt: The Leading Edge, **30**, 1392–1398, doi: 10.1190/1.3672484.

Gueguen, Y., and J. Sarout, 2011, Characteristics of anisotropy and dispersion in cracked medium: Tectonophysics, **503**, 165–172, doi: 10.1016/j.tecto.2010.09.021.

Han, D., A. Nur, and D. Morgan, 1986, Effects of porosity and clay content on wave velocities in sandstones: Geophysics, **51**, 2093–2107, doi: 10.1190/1.1442062.

Han, T. C., A. I. Best, J. Sothcott, and L. M. MacGregor, 2011a, Joint elastic-electrical properties of reservoir sandstones and their relationships with petrophysical parameters: Geophysical Prospecting, **59**, 518–535, doi: 10.1111/j.1365-2478.2010.00940.x.

Han, T. C., A. I. Best, J. Sothcott, and L. M. MacGregor, 2011b, Pressure effects on the joint elastic-electrical properties of reservoir sandstones: Geophysical Prospecting, **59**, 506–517, doi: 10.1111/j.1365-2478.2010.00939.x.

Jakobsen, M., and M. Chapman, 2009, Unified theory of global flow and squirt flow in cracked porous media: Geophysics, **74**, no. 2, WA65–WA76, doi: 10.1190/1.3078404.

Jakobsen, M., J. A. Hudson, and T. A. Johansen, 2003a, *T*-matrix approach to shale acoustics: Geophysical Journal International, **154**, 533–558, doi: 10.1046/j.1365-246X.2003.01977.x.

Jakobsen, M., and T. A. Johansen, 2005, The effects of drained and undrained loading on visco-elastic waves in rock-like composites: International Journal of Solids and Structures, **42**, 1597–1611, doi: 10.1016/j.ijsolstr.2004.07.016.

Jakobsen, M., T. A. Johansen, and C. McCann, 2003b, The acoustic signature of fluid flow in complex porous media: Journal of Applied Geophysics, **54**, 219–246, doi: 10.1016/j.jappgeo.2002.11.004.

Jones, T. D., 1986, Pore fluids and frequency-dependent wave propagation in rocks: Geophysics, **51**, 1939–1953, doi: 10.1190/1.1442050.

Klimentos, T., and C. McCann, 1990, Relationships among compressional wave attenuation, porosity, clay content, and permeability in sandstones: Geophysics, **55**, 998–1014, doi: 10.1190/1.1442928.

Mavko, G., T. Mukerji, and J. Dvorkin, 2009, The rock physics handbook: Tools for seismic analysis of porous media: Cambridge University Press.

Mavko, G., T. Mukerji, and N. Godfrey, 1995, Predicting stress-induced velocity anisotropy in rocks: Geophysics, **60**, 1081–1087, doi: 10.1190/1.1443836.

Nur, A., 1971, Effects of stress on velocity anisotropy in rocks with cracks: Journal of Geophysical Research, **76**, 2022–2034, doi: 10.1029/JB076i008p02022.

Nur, A., and G. Simmons, 1969, Stress-induced velocity anistropy in rock — An experimental study: Journal of Geophysical Research, **74**, 6667–6674, doi: 10.1029/JB074i027p06667.

Pointer, T., E. R. Liu, and J. A. Hudson, 2000, Seismic wave propagation in cracked porous media: Geophysical Journal International, **142**, 199–231, doi: 10.1046/j.1365-246x.2000.00157.x.

Sayers, C. M., 1988, Stress-induced ultrasonic wave velocity anisotropy in fractured rock: Ultrasonics, **26**, 311–317, doi: 10.1016/0041-624X(88)90028-5.

Tatham, R. H., 1982, V_P/V_S and lithology: Geophysics, **47**, 336–344, doi: 10.1190/1.1441339.

Tod, S. R., 2001, The effects on seismic waves of interconnected nearly aligned cracks: Geophysical Journal International, **146**, 249–263, doi: 10.1046/j.1365-246X.2001.00451.x.

Tosaya, C., and A. Nur, 1982, Effects of diagenesis and clays on compressional velocities in rocks: Geophysical Research Letters, **9**, 5–8, doi: 10.1029/GL009i001p00005.

Tucker, M. E., 1991, Sedimentary petrology: An introduction to the origin of sedimentary rocks: Blackwell Scientific Publications.

Xu, S. Y., and R. E. White, 1995, A new velocity model for clay-sand mixtures: Geophysical Prospecting, **43**, 91–118, doi: 10.1111/j.1365-2478.1995.tb00126.x.